Structural, Dielectric, Impedance and Electric Modulus properties of Praseodymium substituted $BaPr_xFe_{12-X}O_{19}$ Nanoparticles synthesized via Sol-Gel Method

Samiullah[1], H. M. Noor ul Huda Khan Asghar[1], Zaheer Abbas Gilani[1*], Muhammad Khalid[2], Awais Ahmed[1], Abdul Kareem Khan[3], Mohammad Rizwan Khan[4], Furhaj Ahmed Sheikh[1], Naushad Ahmad[4], Rosa Busquets[5]

[1]Department of Physics, Baluchistan University of Information Technology, Engineering and Management Sciences (BUITEMS), Quetta, 87300, Pakistan
[2]Department of Physics, University of Karachi, 75270, Karachi
[3]Department of Physics, University of Central Punjab, Bahawalpur Campus, Bahawalpur, Pakistan
[4] Department of Chemistry, College of Science, King Saud University, Riyadh, 11451, Saudi Arabia.

[5]School of Life Sciences, Pharmacy and Chemistry, Kingston University London, Penrhyn Road, KT1 2EE, Kingston Upon Thames, United Kingdom

*Corresponding author
Dr. Zaheer Abbas Gilani, Department of Physics, BUITEMS, Quetta-PK
Email: zaheer.abbas@buitms.edu.pk / zagilani2002@yahoo.com

ABSTRACT

In current research work, Pr^{3+} doped M-type hexaferrites having general formula $BaPr_xFe_{12-x}O_{19}$ ($0.00 < x > 1.00$ with 0.25 steps) was synthesized using Sol-gel technique. The prepared nanoparticles were characterized via XRD for structural Study, FTIR to study the frequency band, SEM was used to investigate the morphological surface, spectroscopic impedance was used to investigate the dielectric properties and VSM was used to study magnetic properties of the ~~ready~~ prepared nanoparticles. XRD pattern for each doping case confirmed the prepared samples having hexagonal phase. The crystalline sizes were determined from 5 – 13 nm range. Lattice constants were measured increase with increasing Pr^{3+} concentration. FTIR analysis was performed to analyze absorption band spectra. LCR meter was used to investigate the impedance, dielectric constant, electric modulus, loss tangent, and A.C conduction of the synthesized samples. From the study of dielectric, properties carried out by Maxwell Wagner model, where a constant of dielectric was found reduced in MHz's of range of frequency, while at high frequency two relaxation peaks was observed by electron hopping of Fe^{2+} to Fe^{3+} ion. Reduction in both real and imaginary impedance caused decreasing trends due to the action of grain boundary. The Pr^{3+} doping has influenced the magnetic properties of the synthesized nanoparticles. The prepared

material exhibited to be hard ferrite, having small crystallite size at high concentration of Pr^{3+} doping. Finally, by the excellent electric and magnetic properties, the prepared particles have a good potential for the applications of recording media, cancer treatment, drug delivery and high frequency devices.

Keywords:
Hexagonal ferrites, FTIR, Pr^{3+}, dielectric constant, Impedance, electric modulus, Infra-red

1. INTRODUCTION

Nano-sized materials due to its small dimensions at large scale as well as physical properties and chemical properties, have a great potential in the field of electronics, medicine, medical and semiconductor industry [1, 2]. In comparison of all ferrite's family, one of the most demanding nano ferrites are hexagonal ferrites. Hexagonal ferrites are ferromagnetic in nature and have been focused due to its simplicity and showing magnetic properties, magneto-optic and super paramagnetism. Multiple sub-types distributed by crystal structure base [3]. Ferrites are classified as a Hard-ferrites and Soft-ferrites. Among these categories hard ferrites are naturally occurring magnetite that possesses a magnetism which is essentially permanent [4].

Among multifarious magnetic materials, M-types of magnetic materials play dominant role due to its high magneto-crystalline anisotropy, saturation magnetization, high superior coercivity, corrosion resistance and chemical stability. Barium ferrites were developed in 1950s and have been under great use due to its tremendous properties in the field of technology, industries, technology, commercial and domestic [5]. M-type magnetic materials are chemically stable and can be saturated at simple approach of magnetization laterally with the c-axis. Such hexagonal ferrites have wide use in high frequency ranges by their strongly magnetically properties. Hexagonal ferrites have hexagonal symmetry in which iron ions are placed at tetrahedral sites such as (FeO_4), trigonal bi-pyramidally such as (FeO_5) and octahedrally such as (FeO_6) with oxygen ions. The M-type magnetic ferrites structure contains 64-ions surrounding, every hexagonal unit cell on 11 specific positions. Furthermore, 24 Fe^{3+} ions are arranged on five various crystallographic locations, in which three are octahedral and their positions are 2a, 12k and 4f2, one is tetrahedral at 4f1 and one trigonal bi-pyramidal at 2b destinations. The inclusion of rare earth metals enhance magnetic properties of hexagonal ferrites [6] linked with the increment of both coercive field with magnetization and magneto-crystalline anisotropy[7, 8].

Previously, X-type of hexaferrites were synthesized having chemical composition of $Sr_{(2-x)}Nd_xNi_2\ Fe_{(28-y)}Co_yO_{46}$ ($0.02 < x > 0.10$ with 0.02 steps) and ($0.1 < y > 0.5$ with 0.1 steps). After getting through preparation process at around 1000°C for 6 hours, where c/a ratio confirmed its structure being X-type of hexaferrites by XRD same was calculated by the FTIR. Grain size and crystal size was measured and found to be as that of concerned ferrites via HRTEM and TEM. The magnetically properties were calculated in concentration giving higher saturation magnetization and lower coercivity showing as prepared particles to be well tolerated microwave absorber [9]. Magnetization and Remanence was found to be completely dependent upon temperature.

Nano-particles rare-earth were doped in a hexagonal ferrite with the chemical composition of $Ba_2NiCoRE_xFe_{28-x}O_{46}$ (x=0.25) by Micro emulsion technique [10]. From XRD characterization, it was found that each compositions had single X-type hexagonal phase same was investigated by FTIR at 500-2400 $cm^{-1,}$ having crystal size between 7-19 nm. Such variations in size are due to cations and anions distribution in the material of hexagonal ferrites [11]. Furthermore, coercivity has been found to have increased with the increasing trends of rare-earth cations. The decreased in saturation magnetization was observed by re-distribution of cations of rare–earth metals on the octahedral sites.

Hexagonal ferrites with chemical composition of $Ba_2NiCoRE_xFe_{28-x}O_{46}$ doped with rare-earth metals. Platelets like structures of hexagonal ferrites were obtained. The dielectric properties showed that the material to be used in higher frequency purposes [12]. The increased of the DC current resistivity from $2.48 \times 108 - 1.20 \times 109\Omega$cm proven such material to be beneficial by lowering eddy current losses and is widely used as a multiple layer indicator device.

M–type of hexagonal ferrites were synthesized via Sol-gel technique which chemical composition is given as $SrFe_{(12-x)}Sm_xO_{19}$ ($0.00 < x > 0.03$ with 0.01 steps). The behavior of samples was investigated to be hard magnets in nature [13]. Where saturation magnetization and remanence were in decreasing trend with substitution. Such prepared materials are beneficial for the applicability in magnetically microwave absorbing materials.

So far, many approaches have been used to prepare nanoparticles of hexagonal ferrites including hydrothermal [14], chemical method [15], co-precipitation [16] [17], mechano-chemical reaction [17, 18], micro-emulsion [19], sol–gel combustion [18], [20], etc. However, all these processes used previously were found expensive and time consuming. In order to make it ease, therefore, used Sol-gel combustion method because of its feasibility and simple to synthesize

nanoparticles of ferrites. Sol-gel technique, also noted for their quick reaction times, affiliated with higher sintering temperature, and showing faster heating rates. Also, through such process, usual and useful materials are economically manufactured. Other benefits of Sol–gel combustion method are lower temperature procedure, good stoichiometry control, lower cost and basic equipment, and creation of the required products [20].

In this study, the Praseodymium Pr^{3+} doped hexagonal ferrites were prepared chemically composed as $BaPr_xFe_{12-X}O_{19}$ ($0.0 < x > 1.0$ with 0.25 steps) through Sol-gel technique.

2. METHODOLOGY

$BaPr_xFe_{12-X}O_{19}$ ($0.0 < x > 1.0$ with 0.25 steps) hexagonal ferrites were prepared by Sol gel technique. All the chemicals in appropriate amount were dissolved in distilled water in a separate beaker for five samples. The first sample was put on the hotplate and stirred to get the homogenous and aqueous solution. Adjusted the temperature at 80°C and made continues stirring till formation of sol. Further heat the solution till half an hour developed the formation of gel. After the gel is formed, the temperature of hotplate was set at 1200°C. While attaining the said temperature, the gel started to convert into burning gradually and fully burnt by adopting the shape of ashes of fire. The formed materials were grinded by mortar and pestle in order to obtain refine powder. The samples were then annealed in a muffle furnace on 800 around 4 hours, later the annealing, the subject material was made pallets for determining its resistivity. Pallets were made by subjecting the material by applying 05 Tons compressed forced. Pallets with 0.250g of weight, 0.20mm of thickness and 1.05 of its diameters were obtained and kept separately in a pallet boxes.

The XRD of every prepared composition were carried out using The FTIR analysis was carried out through Nicolet TM iS50 FTIR spectrometer of 400 cm^{-1} – 1000 cm^{-1} frequency range. The LCR meter was used to measure impedance, dielectric constant, and electric modulus, as well as investigate parallel and series capacitance and resistance. The pellets were dried in a vacuum at 100 °C before the electric measurement to eliminate any humidity effects. The materials' electric characteristics were measured using a Wayne Kerr LCR meter, model 6520P. By applying five tons of pressure for two minutes with press machine, dry powder was turned into pellets with a thickness of 0.20 mm and a diameter of 1.05 mm.

3. RESULTS AND DISCUSSION

3.1. XRD analysis

In Figure 1, XRD patterns of all compositions of Pr^{3+} doped have been investigated, all the values of XRD had been observed and displayed here of $BaFe_{12}O_{19}$ on the basis of ICPD card, which gave us values of d at planes such as (107). Furthermore, here all the samples showed single phase hexagonal ferrites having no residuals of the original constituent's oxides. Through the graphs we infer that Pr^{3+} ions have thoroughly mixed with the lattice of the hexaferrites [21].

The value varies from composition to composition and with the inclusion of Pr^{3+}, the value of V increases and the shifting of peaks are due to the varying ionic radii of the Pr^{3+} and Fe^{3+} that is 1.086 Å and 0.67 Å correspondingly. Once Pr^{3+} is doped in the hexaferrites, the change occurred in the lattice distortion.

Some extra peaks can be seen on the graphs which are due to some sort of un-reacted constituents or can be said as impurities. In addition to this, the lattices constant *a* & *c* were measured [19] via following relation:

$$1/d2hkl = 4(h2 + hk + K2)/3a2 + l2/c2 \qquad (1)$$

In above equation, (d^2_{hkl}) represents the inter planer distance where h, k, l is known as Miller indices. By addition of rare-earth metal, the variations were found in the lattices parameters *a* & *c* by the difference of radii of ions of the rare earth metal with iron.

3.1.1 Pr^{3+} Concentration verses Lattice constants a and c

The lattice constant (*a*) observed varies from 5.84Å to 6.00 Å as illustrated in Table1. With different concentration it has given different increasing and decreasing trends. The up and downs in the Figure 2 are due to the varying radii of ions of Pr^{3+} & Fe^{3+} which are 1.086 Å and 0.67 Å correspondingly. In all hexagonal ferrites 'c' and 'a' are changing. Therefore, lattice parameter *c* is called major-axis and '*a*' known as minor-axis [22] [23].

Additionally, lattice parameter 'c' has given regular increase in the trend on the basis of ionic radius of Pr^{3+} varied from that of Fe^{3+}. Here, the values of a lattice constant 'c' vary between 22.9 to 23.9 Å. Such varying trends are because of the variation among ionic radii of available and substituted material in concentration.

3.1.2 Pr^{3+} Concentration onto Crystallite Size

The crystalline sizes were measured via the relation known as Scherrer formula [20].

$$S = k\lambda/B\cos\theta \quad (2)$$

In the above equation, S is crystallite size, λ is wavelength having value as 1.5406Å, K is constant, which values as 0.94Å, β represents FWHM, θ is used to represent the angle of most intense peak. The crystallite sizes were calculated depending on the Pr^{3+} doping as summarized in Table. 1. The crystalline sizes with doping from 5 to 13nm range was found. Figure 3 shows the result of Pr^{3+} doping on the crystalline sizes as showing the decreasing trend with increasing the concentration.

3.1.3 Pr^{3+} Concentration Verses Volume of the Unit Cell

The relation was used to compute the cell volume given as.

$$V = a^2 c \sin 120° \quad (3)$$

Or

$$V = a^2 c\ (0.866) \quad (4)$$

Where, *a* & *c* are the lattice parameters and sin120°gives an angle between these lattice constants. The changes observed has been justified by the relation given in Table1.

3.1.4 Pr^{3+} Concentration onto X-Ray Density

Furthermore, the following relation was used to compute density of X-ray, given as.

$$\delta_x = 3M/NV \quad (5)$$

In equation 5, M represents the molar mass, volume is represented by V and Avogadro's number is represented by N in the above equation.

In Figure 4, an increase has been noted in the X-Ray density of the concerned hexaferrites doped with rare earth metal, the reason behind increasing trend of X-ray density is molecular weight of material doped with varying proportion. Here it is to mention the molecular weight of Fe^{3+} is 55.84g/mol and Pr^{3+} are 329.813g/mol respectively.

3.1.5 Pr^{3+} Concentration onto Bulk Density

The following equation was used to compute the bulk density.

$$\delta = m/\delta r^2 h \quad (6)$$

Mass is represented by m, thickness by h and r is pellets radius.

Figure 5 evidences a sudden increase in the bulk density with increasing order of doped material in the concentration followed by an approximate linearity in the trend values given in Table 1. The bulk density values are comparably small compare to that of density of X-rays. But both have

given increasing trends.

3.1.6 Concentration verses Lattice Strain and Micro Strain

The Lattice strain is generally calculated by a formula, which is known as Stokes-Wilson equation. Mathematically, it is expressed as.

$$(Lattice\ Strain)\ \varepsilon = \beta/4*\tan(\theta)\ 10^{-3} \quad (7)$$

However, Micro strain is measured by the following relation, which is mathematically expressed as;

$$Micro\ strain = \beta*\cos(\theta)/4*10^{-3} \quad (8)$$

Additionally, while going through the illustrated Figure 6, a regular decrease has been noted in both the parameters (Lattice Strain and Micro Strain), and both the trends has given approximately same values at the initial and final points and varied in the middle illustrated in Table 1.

3.2. FTIR analysis

The formation of hexagonal phases of all compositions are get confirmed by the FTIR. It gives us idea about the taking place of doped particles in the octahedral and tetrahedral sites which cause dislocation of cations distribution; such changes in the composition lead us to chemical changes. FTIR spectra of $BaPr_xFe_{12-X}O_{19}$ ($0.0 < x > 1.0$ with 0.25 steps) can be better understood by the following spectra obtained by FTIR. In the given spectra two main frequency bands are under focus both of which have high frequency bands of approx. $520cm^{-1}$ and low frequency band approx. $425cm^{-1}$ in the hexagonal ferrites due to extending vibrations of (Fe-O) bond in the crystal lattice resulting that the investigated material is hexagonal ferrites of M-type Such shift in the bands is attributed due to size of grain and parameters of lattice as shown in table 2.

In the above figure 7, the spectra of FTIR ranging from 400-$1000cm^{-1}$. The higher frequency bands are attributed to tetrahedral site of intrinsic stretching vibrations of metal while lower frequency band belongs to the octahedral stretching bands [24]. Table expresses the different frequencies obtained by increasing the Pr^{3+} content [25]. The stretching vibrations of crystals on tetrahedral and octahedral are influenced by changing in lattice parameter. In the current spectra, by increasing a doped material of Pr^{3+}, the octahedral peaks shifted to slightly lower values. Conversely, in tetrahedral absorption peaks the addition of doped material of Pr^{3+} causes the peaks to shift to lower frequency side as well.

3.3. Dielectric

Such properties of hexagonal ferrites are thoroughly studied by Conductivity spectroscopy. The polarization takes place when a DC voltage is applied across the sample. However, for bulk material, two probe methods were applied for conduction mechanism, while four probe for studying the surface morphology of the material [26]. AC behavior is considered a thorough step to study conduction mechanism of ferrites.

3.3.1 Real and imaginary parts of impedance

The electrical behavior of the hexagonal ferrites is completely understood by using its impedance analysis [26]. As impedance acting as a vital role in the description of dielectric properties of materials. Impedance of a material is wholly dependent upon the frequency applied. Figure 8 and 9 exhibits the impedance as a function of frequency. Here real and imaginary parts are calculated as:

$$Z' = R = |Z|\cos\theta z \quad (9)$$

$$Z'' = X = |Z|\sin\theta z \quad (10)$$

In the figures, real and imaginary parts have shown decreasing trends by increment of frequencies, and it finally shows steady behavior which is attributed by release of space charges. Such decrease of real and imaginary parts is because of improvement of conductivity with the increase in frequency. Such drop in space charge polarization leads to the frequency in peak is known as Relaxation merger of curves at high frequency.

The attainment of relaxation time is due to the highest value of real and imaginary parts of impedances. This is given by,

$$t = t_0 \exp(E_a/K_B T) \quad (11)$$

Such shift of frequencies with respect to the temperature is the result of increased hopping of localized charge carriers as studied by [27]. So as to explain it thoroughly, we use different methods such as, dielectric loss, permittivity, impedance etc. the relation of which can be better understood by the following:

$$\tan\delta = \varepsilon''/\varepsilon' = Y''/Y' = Z''/Z' = M''/M' \quad (12)$$

Figure 8 shows the behavior of impedance with respect to frequency from 5.5 GHz to 10 GHz of range respectively. The impedance of hexagonal ferrites is improved by addition of rare earth compositions [26]. The whole behavior of impedance is also given in table 4..

3.3.2 Dielectric Constant and complex dielectric

The relative speed of e.m waves in the material is obtained by the measurement of values of dielectric constants of the concerned material [28, 29].

Such plot relation between frequency and constant of dielectric and Complex dielectric is depicted in the above figures 10 (a) and 10 (b), showing the difference of the real (έ) and imaginary part of dielectric constants as a function of frequencies varying ranges $BaPr_xFe_{12-X}O_{19}$ ($0.0 < x > 1.0$ with 0.25 steps). Dispersion with frequency has been obtained from both the graphs of real and complex part of the dielectric constant. Both real and complex part of dielectric constant values higher at lower frequencies and decrease rapidly by increase of frequencies in all samples which is considered as a universal trend for all the ferrites as depicted in table 3. Such behavior of dispersion shows the agreement of Maxell Wagner interfacial polarization with the Koop's phenomenological theory [30, 31]. The exchange of ions between Iron (Fe^{3+}) and Praseodymium (Pr^{3+}) give rise to the dispersion to the direction of electrical fields, indicates the polarization. Such polarization reduces by the increment of frequencies and raises a steady value. The adoption of constant value is because of ions exchange not following the alternating field. It is additionally observed that at above 1.5 GHz frequency, the trends for all samples show a sudden increase in both dielectric and Complex Dielectric, indicating that the samples approaches its frequency of resonance. Such resonance might be of a mechanical nature involving the whole samples in a natural vibrational mode. At such point it is inferred that samples reach their resonance frequency. At high frequencies the electric polarization is liable for the hopping Process [32]. However, at higher frequency the interfacial and dipolar polarization perform a dominant role. Additionally, at lower frequencies, higher values are observed may be due to the inclusion of Praseodymium Ions interacting with the vacancies of Oxygen Ions and boundaries defects within grains. Furthermore, such reduction in the frequency of real and complex part of dielectric constant is due to the specimen contributing and legging behind the electric field applied. Maximum dielectric loss is given by a relation $\omega_{max}\tau=1$ [33].

3.3.3 Relation between Frequency and Tangent Loss

The ratio obtained by the relation of current loss and current charging is known as Tangent loss or the ratio of complex dielectric to real dielectric constant is known as Tangent loss. Tangent loss is dependent of various factors such as stoichiometry, density of charge carriers, structure, preparing method and materials calcination temperature [34]. ingredients having high values of

conductance show higher dielectric loss [35]. In figure 11, the relation of tangent loss with respect to increment of frequencies range, it is discussed that the tangent loss decreases by increase of frequencies [36], and all the concentrations show hump at higher frequencies which is given in table 3. At lower frequencies of the electrical field, electrons of the doped material follow the field and hence a drop in a graph is seen, and tangent loss is extreme. At high frequency of the electrical field, the electron hopping frequencies interchange between Fe3+ and Pr3+do not obey the field outside certain frequencies and hence loss is maximum. The widening of the dissipation curves with increasing frequency for all samples is related to the dipoles' alternating fields direction. [37, 38]. The tangent loss is in contract with the Koop's phenomenological theory which is higher at lower frequencies [33]. Thus, by the increase in compositions resonance frequency is decreased.

3.3.4 Log of Frequency affecting electric modulus

Figure 12 and 13 discusses the variations in dielectric constant verses frequency, where the dispersion of different varying compositions is seen by increase in temperature and frequency. Such change in dielectric constant is not constant rather it gives different varying values at different points. Such decrease in dielectric is due to failure of electrical dipole to obey by the changes of applied AC field. The increase in temperature increases dielectric constants as it enables more dipole to be oriented along with the field which results increase in dielectric constants as given in table 4. Here the variation is based upon the relation of Maxwell-Wagner two model layers for interfacial polarization and Koop's theory. Such state that " A huge number of conducting grains make up a substance, separated by low conducting grain boundary." When a charge is functional the grains can simply pass through the grain boundaries and accumulate at the grain boundary while producing large polarization and high dielectric constant [27]. Dielectric loss occurs as a result of the absorption of electric energy utilized to rotate dipolar molecules. The dangling bonds on the surface layers are reactive and may absorb gases like as oxygen and nitrogen, increasing dielectric loss.

3.3.5 Frequency verses AC Conductivity

AC conductivity is basically the number of electric currents in the given samples of material. The relation between frequency and AC conductivity of the composition of hexagonal ferrites is elaborated in the figure 14.

The observed phenomena in the graph depicted from the relation of frequency and AC conductivity, showing that increasing trend at low frequency and it shows an increasing order at the increasing frequencies also described in table 4. As the conduction of any material is dependent on dielectric polarization. Therefore, same planes and similar area is found for each of the composition. The high frequencies region, the grains affection then increasing dispersion are at the octahedral sites performs a major role in conduction [29]. Therefore, the rise in conductivity with respect to the composition is directly depending upon it and in total agreement with the Koop's law [39]. However, the increase in conductivity depends upon the porosity and dielectric properties as well [40]. The formula was used to compute the AC conductivity.

$$\sigma AC = \omega \varepsilon 0 \varepsilon' (tan\, \delta) \quad (13)$$

By a rise in externally applied frequency, the AC conductivity improves. As noted, there is a link between the dielectric and conduction mechanisms in ferrites [29], assuming that hexaferrite conduction is analogous to the polarization mechanism caused by hopping events. The electron hoping of iron Fe^{3+} is responsible for the conduction in hexaferrites. Same is justified here in this research work by the substitution of Pr^{3+} ions in M-type of hexaferrites.

3.4. Magnetic properties

From the From the data obtained from VSM was used for investigation of magnetic effect at 10000°C from the hysteresis loop. The variable retentivity H_r, Coercivity, and saturation magnetization were obtained from the plots and data of VSM. All these parameters such as saturation magnetization, coercivity and magnetization were obtained via hysteresis loop with varying/ increasing proportion of Pr^{3+} in the concentration. Well saturated hysteresis loop is seen as a result. However, the mix up of align rare-earth metals results in the changed form of hysteresis loop.

Here, it has been determined that initially with lower proportion of doped material, $BaFe_{12}O_{19}$ is soft ferrites. Figure 15 shows that increment of doping content of Pr^{3+} leads to increase in M_s and M_r values. However, a sudden drop has been noted after the regular repetition. Net magnetization is obtained by the mean values of sub-lattices magnetization of A and B. On the other hand, Coercivity of the material has been studies changing between two peaks. It will be either giving one value or the other. Furthermore, the anisotropic constant depends upon H_c and M_s. From the obtained data regular increase has been seen followed by a sudden drop at x = 0.75

concentration.

Anisotropic constant is deduced by the relation given as

$$(Anisotropy\ Constant)\ k = H_c * M_s / 0.96 \qquad (14)$$

In the relation expressed above, K represents Anisotropic constant.

In the relation, the magneto numbers are obtained by the relation,

$$(Bohr\ Magneto)\ n_B = M * M_s / 5585 * x\text{-}ray\ density \qquad (15)$$

In the relation, it can be interpreted that the relation between concentration with Bohr magneton and Anisotropic constant goes parallel and almost follow the same trends as displayed in Figure 16 and shown in table 5.

In the M-type of Hexagonal ferrites are known for Fe^{3+} having 05 Bohr magnetons which gives total magneton as 20. Thus resultantly seven Fe^{3+} possess magnetic moments with each sitting at 12K (↑) and 4f2 (↓) sub lattices belonging to Octahedral sites, one iron ion at 4f1 (↓) belong to trigonal bipyramidal sites and two at tetrahedral sites at 4f1 (↓). Here arrow heads represent direction of the magnetic moments due to Fe^{3+} ions [41].

3.4.1 Relation between concentration and grain size

From the figure 17, the relation of concentration with grain size can be easily interpreted, while increasing the proportion of x in the concentration, a regular decrease in the grain size is noted which is because of increase in grain size. Same behavior of decrease in coercivity is observed at microstructure. It further justifies the inverse nature of coercivity with respect to grain size [42]. The diameter of grain size Pr^{3+} and Fe^{3+} is 1.086 Å & 0.67 Å. Thus, the reduce in grain size, number of atoms per unit volume will be increased.

3.4.2 Relation between concentration verses Saturation Magnetization and Retentivity

By figure 18, the values of saturation magnetization and Retentivity via loops of hysteresis at different proportion of the Pr^{3+} doped concentration has been displayed where the saturation magnetization and Retentivity go parallel by increasing proportion of doped rare earth metal in hexaferrites. Thus causes magnetic properties of hexagonal ferrites significantly [41] as given in table 5.

3.4.3 Relation between concentration verses Remanence R, Coercivity Hc.

Here from the figure 19, it is interpreted that the Remanence and Coercivity with respect to

concentration (x), goes parallel. Initially, the saturation magnetization is seen to be increased and coercivity is seen followed by the parallel decrease of both the parameters, and then again, an increase is noted. However, for the first doping where x = 0.00, the trend is different from each other. Moreover, figure 20, 21 and 22 gives the SEM images with histogram of SEM and EDX. Table 6 gives the elemental analysis of the given samples.Such micrographs show the presence and stacking of granular structure finely distributed on the surface of the material.

4. CONCLUSION

Praseodymium (III) Nitrate Pr^{3+} doped in hexagonal ferries having chemical composition of $BaPr_xFe_{12-X}O_{19}$ ($0.00 < x > 1.00$ with 0.25 steps) synthesized via Sol-gel technique. a notable variance in parameters have been noted in Structural, electric, and properties of dielectric for hexaferrites. XRD enabled us to study the structural behavior of hexaferrites such as lattice sizes, lattice constants a & c, bulk density and X-ray density. Through FTIR spectroscopy, a shifting of frequencies ranges were investigated by the inclusion of Praseodymium (III) Nitrate Pr^{3+}. In dielectric properties of a material, dielectric constant, Complex dielectric, Tangent loss, conductivity of AC, Impedance, frequency and dielectric loss were calculated. Where the dielectric impedance both real and complex part were decreased by increase in frequencies because of release of space charges and causing improvement in conductivity. In addition, dielectric constants exhibited sudden drop followed by dispersion by increase in frequencies. Such dispersion is attributed to interchange of ions among the atoms of Fe^{3+} and Pr^{3+}. The increase in temperature increases dielectric constants as it enables a growing number of dipoles to be aligned with the field resulting increase in dielectric constants. Such variation is based upon the Maxwell-Wagner two model layers for interfacial polarization and Koop's phenomenological theory. Some planes and similar region were observed for each composition. The high frequencies region, the grains affection and increasing dispersion are at the octahedral sites performs major role in conductivity. Such unique properties of nanoparticles of hexagonal ferrites will be useful in high frequency applications. For magnetic properties, we used VSM through which change in saturation magnetization, Coercivity and remanence, retentivity, squareness ratio, Bohr magneton and Anisotropic constants have been calculated and noted. Such behavior of ferrites showed it as a hard ferrite, which can be used in high frequency material and applications.

Acknowledgement

The authors would also like to thank the Researchers Supporting Project No. (RSP-2021/138) King Saud University, Riyadh, Saudi Arabia.

REFERENCES

1. Wang, K., et al., *First-principles study on magnetoelectric coupling effect of M/BiFeO3 (M = Co, Fe) multiferroic superlattice.* Vacuum, 2019. **165**: p. 105-112.
2. Wang, Z., et al., *Substitution effects on ferroelectric, leakage current and anti-fatigue characteristic of Bi4-xSbxTi3O12thin films.* Crystal Research and Technology, 2016. **51**(12): p. 696-701.
3. Pullar, R.C., *Hexagonal ferrites: a review of the synthesis, properties and applications of hexaferrite ceramics.* Progress in Materials Science, 2012. **57**(7): p. 1191-1334.
4. Wang, Z., et al., *Effects of 60Co γ-ray irradiation on microstructure and ferroelectric properties of Bi3. 25La0. 75Ti3O12 thin films.* Nuclear Instruments and Methods in Physics Research Section B: Beam Interactions with Materials and Atoms, 2016. **366**: p. 1-5.
5. Wang, Z., et al., *Effects of 60 Co γ-ray irradiation on microstructure and ferroelectric properties of Bi 3.25 La 0.75 Ti 3 O 12 thin films.* Nuclear Instruments and Methods in Physics Research Section B: Beam Interactions with Materials and Atoms, 2016. **366**: p. 1-5.
6. *<Amin, M. B. James, J. R. Techniques for utilization of hexagonal ferrites in radar absorbers. Part 1 Broadband planar coatings. Radio and Electronic Engineer, 51, 209-218..pdf>*.
7. Al-Hilli, M.F., S. Li, and K.S. Kassim, *Structural analysis, magnetic and electrical properties of samarium substituted lithium–nickel mixed ferrites.* Journal of Magnetism and Magnetic Materials, 2012. **324**(5): p. 873-879.
8. Singh, R.P. and C. Venkataraju, *Effect of calcinations on the structural and magnetic properties of magnesium ferrite nanoparticles prepared by sol gel method.* Chinese Journal of Physics, 2018. **56**(5): p. 2218-2225.
9. Sadiq, I., et al., *Structural, infrared, magnetic and microwave absorption properties of rare earth doped X-type hexagonal nanoferrites.* Journal of Alloys and Compounds, 2013. **570**: p. 7-13.
10. Umer, A., et al., *Selection of a suitable method for the synthesis of copper nanoparticles.* Nano, 2012. **7**(05): p. 1230005.
11. Majeed, A., et al., *Structural elucidation and magnetic behavior evaluation of rare earth (La, Nd, Gd, Tb, Dy) doped BaCoNi-X hexagonal nano-sized ferrites.* Journal of Magnetism and Magnetic Materials, 2016. **408**: p. 147-151.
12. Majeed, A., et al., *Morphological, Raman, electrical and dielectric properties of rare earth doped X-type hexagonal ferrites.* Physica B: Condensed Matter, 2016. **503**: p. 38-43.
13. Yasmin, N., et al., *Influence of samarium substitution on the structural and magnetic properties of M-type hexagonal ferrites.* Journal of Magnetism and Magnetic Materials, 2018. **446**: p. 276-281.
14. Srivastava, M., S. Chaubey, and A.K. Ojha, *Investigation on size dependent structural and magnetic behavior of nickel ferrite nanoparticles prepared by sol–gel and hydrothermal methods.* Materials Chemistry and Physics, 2009. **118**(1): p. 174-180.
15. Wang, J., et al., *Improved ferromagnetic properties of electrospun NiFe2O4 with tunable morphology: from multiparticle-chain to single-particle-chain.* Journal of nanoparticle research, 2014. **16**(5): p. 1-11.
16. Dehghanpour, H.R., *Nickel ferrite nanoparticle generation by combustion method and the*

nanoparticle structural and magnetic characterization and the effect of ball milling. IEEE Transactions on Magnetics, 2016. **53**(1): p. 1-5.
17. Kumar, K.V., D. Paramesh, and P.V. Reddy, *Effect of aluminium doping on structural and magnetic properties of Ni-Zn ferrite nanoparticles.* World Journal of Nano Science and Engineering, 2015. **5**(03): p. 68.
18. Kumar, E.R., et al., *Magnetic, dielectric and sensing properties of manganese substituted copper ferrite nanoparticles.* Journal of Magnetism and Magnetic Materials, 2014. **355**: p. 87-92.
19. Ganure, K.A., et al., *Synthesis and characterization of lanthanum-doped Ni-Co-Zn spinel ferrites nanoparticles via normal micro-emulsion method.* Int. J. Nanotechnol. Appl, 2017. **11**(2): p. 189-195.
20. Reddy, M.P., R. Shakoor, and A. Mohamed, *Auto combustion synthesis, microstructural and magnetic characteristics of nickel ferrite nanoparticles.* Indian J. Sci. Technol, 2017. **10**: p. 13.
21. Amin, M. and J. James, *Techniques for utilization of hexagonal ferrites in radar absorbers. Part 1: Broadband planar coatings.* Radio and Electronic Engineer, 1981. **51**(5): p. 209-218.
22. Dhage, V.N., et al., *Influence of chromium substitution on structural and magnetic properties of BaFe12O19 powder prepared by sol–gel auto combustion method.* Journal of Alloys and Compounds, 2011. **509**(12): p. 4394-4398.
23. Dimri, M.C., S.C. Kashyap, and D. Dube, *Electrical and magnetic properties of barium hexaferrite nanoparticles prepared by citrate precursor method.* Ceramics international, 2004. **30**(7): p. 1623-1626.
24. Ahmed, M., N. Okasha, and R. Kershi, *Influence of rare-earth ions on the structure and magnetic properties of barium W-type hexaferrite.* Journal of Magnetism and Magnetic Materials, 2008. **320**(6): p. 1146-1150.
25. Majeed, A., et al., *Structural elucidation and magnetic behavior evaluation of rare earth (La, Nd, Gd, Tb, Dy) doped BaCoNi-X hexagonal nano-sized ferrites.* Journal of Magnetism and Magnetic Materials, 2016. **408**: p. 147-151.
26. Tahir Farid, H.M., et al., *Structural and dielectric properties of copper-based spinel ferrites.* The European Physical Journal Plus, 2018. **133**(2).
27. Joshi, J.H., et al., *Dielectric relaxation, complex impedance and modulus spectroscopic studies of mix phase rod like cobalt sulfide nanoparticles.* Materials Research Bulletin, 2017. **93**: p. 63-73.
28. Anis-ur-Rehman, M. and G. Asghar, *Variation in structural and dielectric properties of co-precipitated nanoparticles strontium ferrites due to value of pH.* Journal of Alloys and Compounds, 2011. **509**(2): p. 435-439.
29. Asghar, G. and M. Anis-ur-Rehman, *Structural, dielectric and magnetic properties of Cr–Zn doped strontium hexa-ferrites for high frequency applications.* Journal of Alloys and Compounds, 2012. **526**: p. 85-90.
30. Wu, Y., et al., *Pr3+-substituted W-type barium ferrite: preparation and electromagnetic properties.* Journal of Magnetism and Magnetic Materials, 2012. **324**(4): p. 616-621.
31. Lead, J.R. and K.J. Wilkinson, *Aquatic colloids and nanoparticles: current knowledge and future trends.* Environmental Chemistry, 2006. **3**(3): p. 159-171.
32. Hussain, S. and A. Maqsood, *Structural and electrical properties of Pb-doped Sr-hexa ferrites.* Journal of Alloys and Compounds, 2008. **466**(1-2): p. 293-298.

33. Asif Iqbal, M., et al., *High frequency dielectric properties of Eu+3-substituted Li–Mg ferrites synthesized by sol–gel auto-combustion method.* Journal of Alloys and Compounds, 2014. **586**: p. 404-410.
34. Auwal, I.A., et al., *Dielectric properties, cationic distribution calculation and hyperfine interactions of La3+ and Bi3+ doped strontium hexaferrites.* Ceramics international, 2016. **42**(7): p. 9100-9115.
35. Meena, R., S. Bhattachrya, and R. Chatterjee, *Complex permittivity, permeability and wide band microwave absorbing property of La3+ substituted U-type hexaferrite.* Journal of Magnetism and Magnetic Materials, 2010. **322**(14): p. 1923-1928.
36. *<Abo, E. A. A., El Nimr, M. K., El Kony, D., AL-Hammadi, A. H. . Dielectric and magnetic permeability behavior of BaCo 2-x Ni x Fe 1 6 O 2 7 W-type hexaferrites. Journal of Magnetism and Magnetic Materials,.pdf>*.
37. Iqbal, M.J., M.N. Ashiq, and I.H. Gul, *Physical, electrical and dielectric properties of Ca-substituted strontium hexaferrite (SrFe12O19) nanoparticles synthesized by co-precipitation method.* Journal of Magnetism and Magnetic Materials, 2010. **322**(13): p. 1720-1726.
38. Wang, S., et al., *Preparation and properties of yttria doped tetragonal zirconia polycrystal/Sr-doped barium hexaferrite ceramic composites.* Materials Science and Engineering: B, 2015. **193**: p. 91-96.
39. Ali, I., et al., *Role of grain boundaries in the conduction of Eu–Ni substituted Y-type hexaferrites.* Journal of Magnetism and Magnetic Materials, 2014. **362**: p. 115-121.
40. Murthy, V. and J. Sobhanadri, *Dielectric properties of some nickel-zinc ferrites at radio frequency.* physica status solidi (a), 1976. **36**(2): p. K133-K135.
41. Luo, J., *Structural and magnetic properties of Nd-doped strontium ferrite nanoparticles.* Materials Letters, 2012. **80**: p. 162-164.
42. Singh, C., et al., *Hysteresis analysis of Co–Ti substituted M-type Ba–Sr hexagonal ferrite.* Materials Letters, 2009. **63**(22): p. 1921-1924.

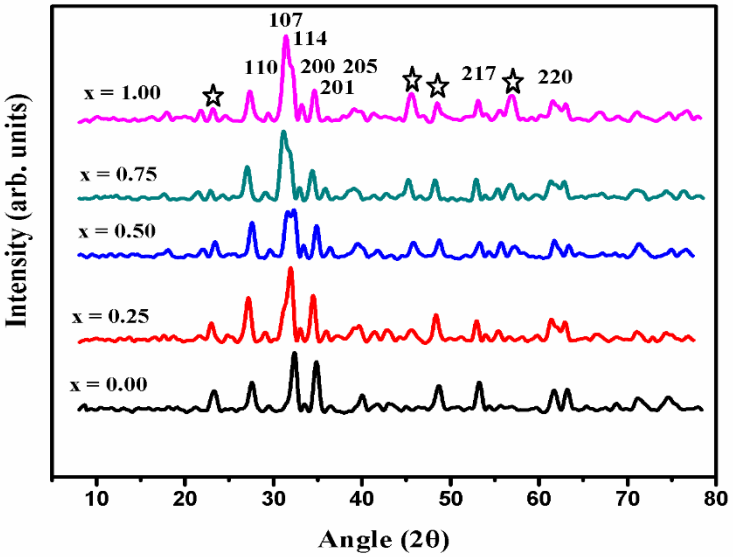

Figure 1. XRD patterns of $BaPr_xFe_{12-x}O_{19}$

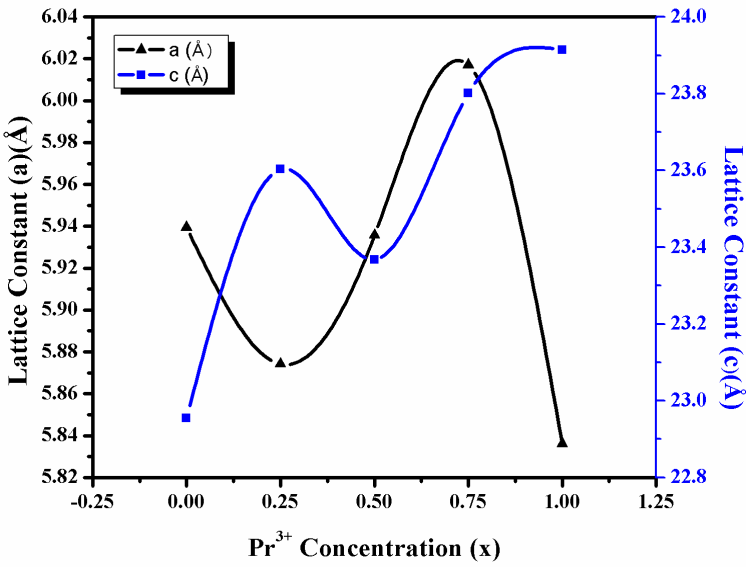

Figure 2.Pr^{3+}Concentration and Lattice constants a and cof $BaPr_xFe_{12-x}O_{19}$(X= 0.00, 0.25, 0.50, 0.75, 1.00)

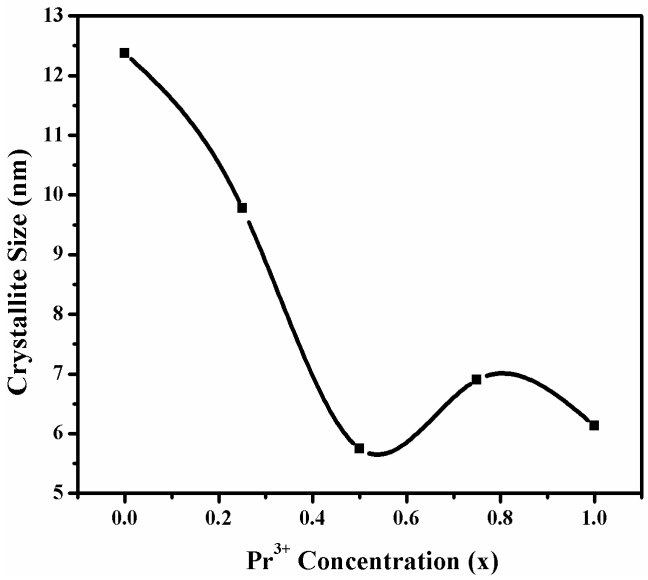

Figure 3.Pr^{3+}Concentration verses Crystal Size

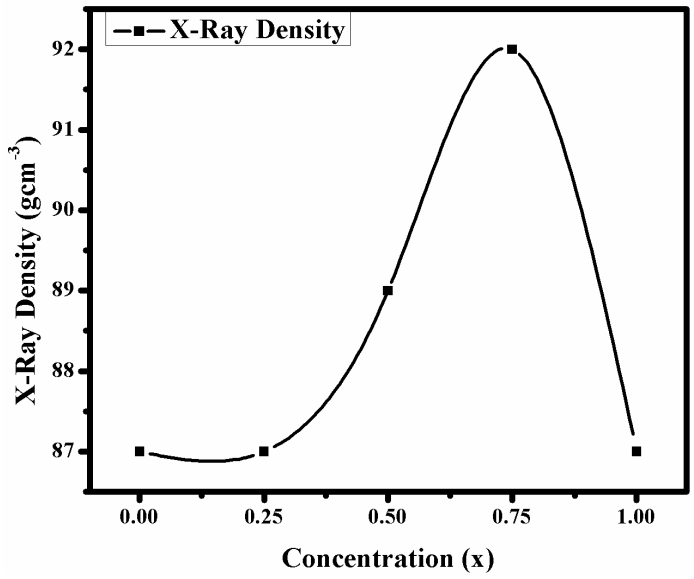

Figure 4.Pr^{3+}Concentration Verses X-ray Density

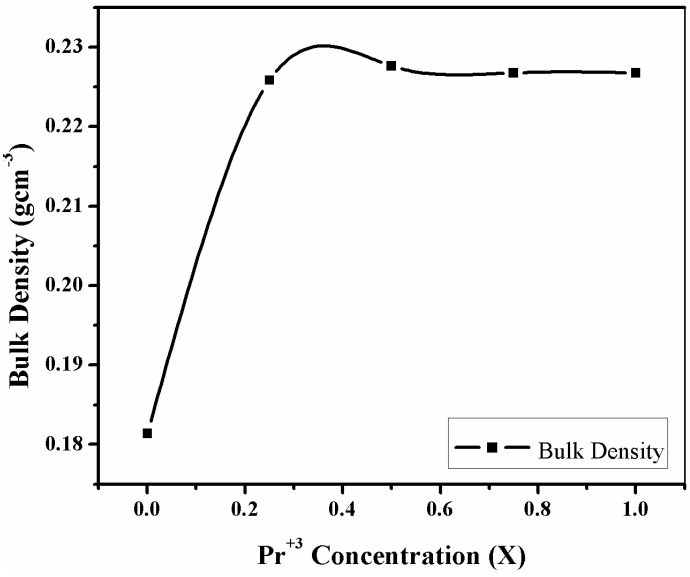

Figure 5.Pr^{3+}Concentration onto Bulk density

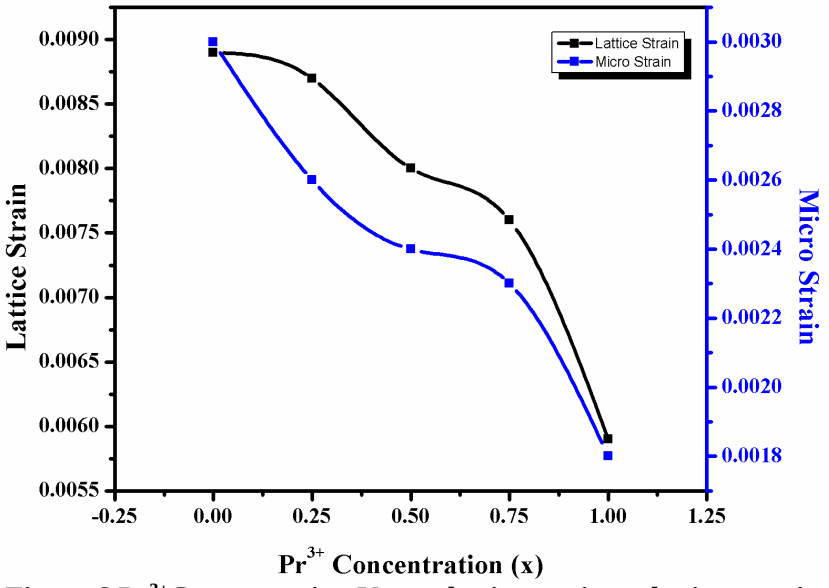

Figure 6.Pr^{3+}Concentration Verses lattice strain and micro strain

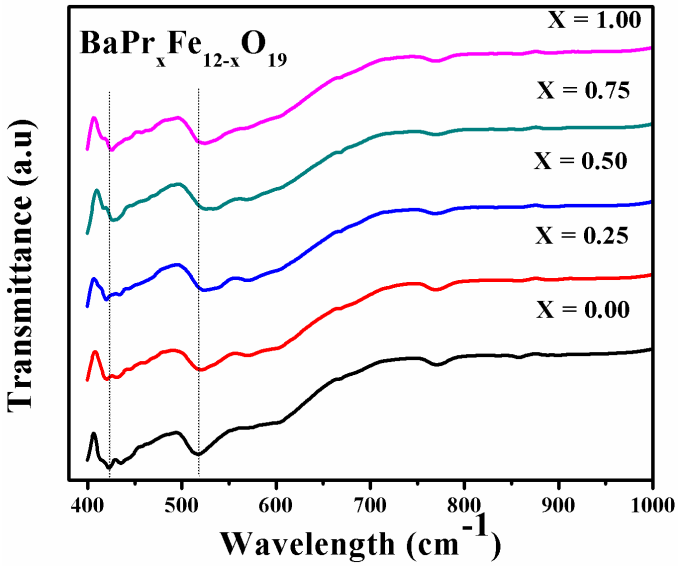

Figure 7. FTIR spectra of $BaPr_xFe_{12-X}O_{19}$

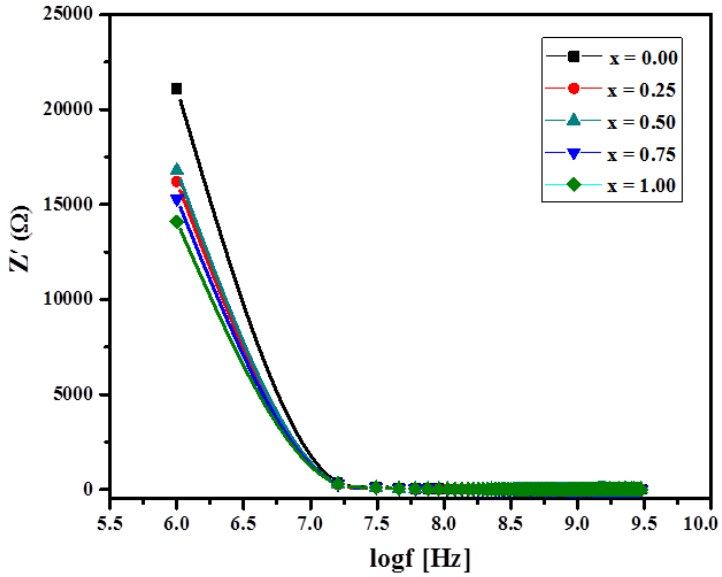

Figure 8. Effect of Frequency on Real part of Impedance

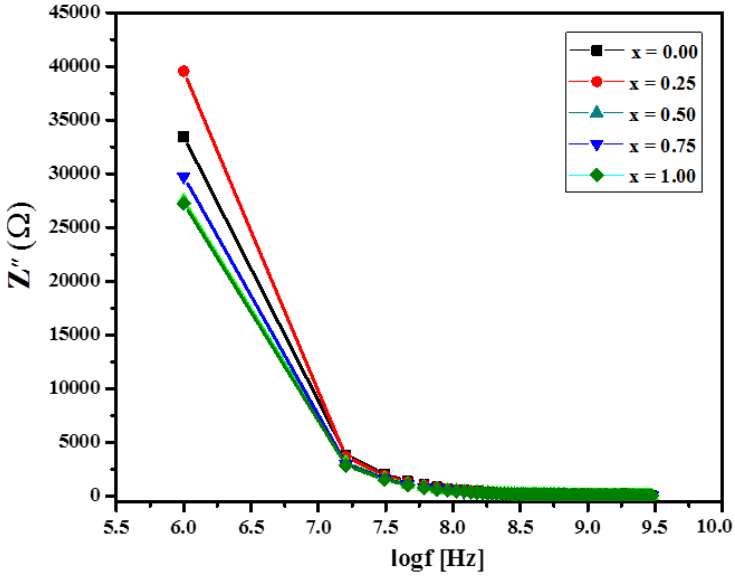

Figure 9. Effect of Frequency on the Real and Imaginary parts of Impedance

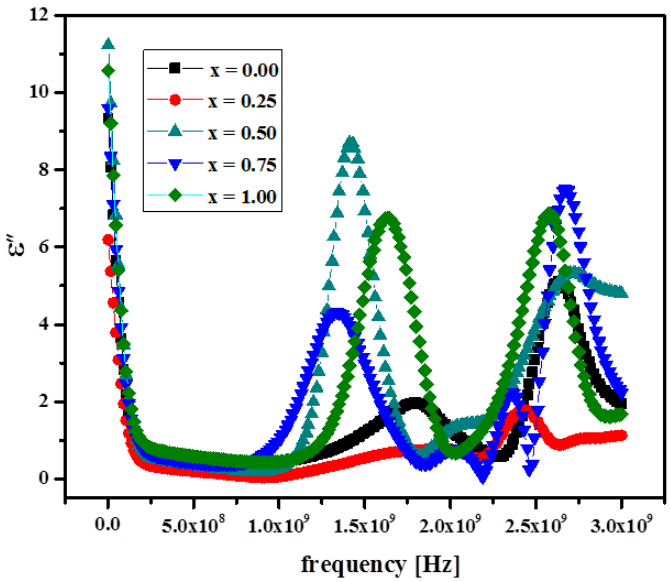

Figure 10(a). Effect of Frequency on Complex dielectric Constant

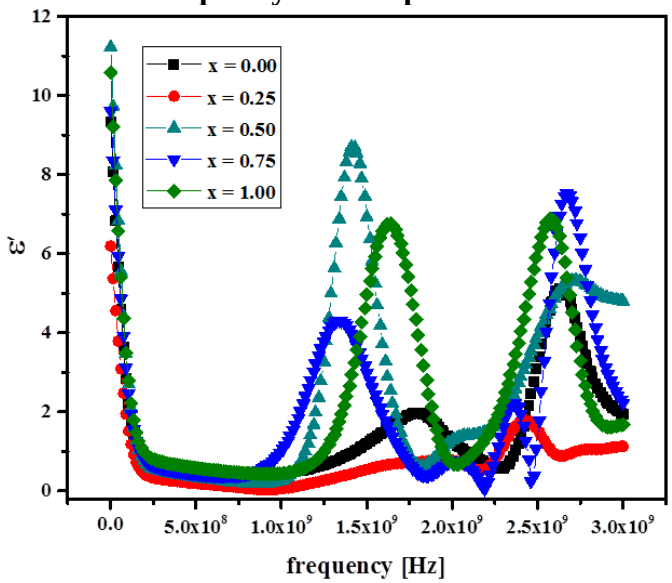

Figure 10(b). Effect of Frequency on dielectric constant

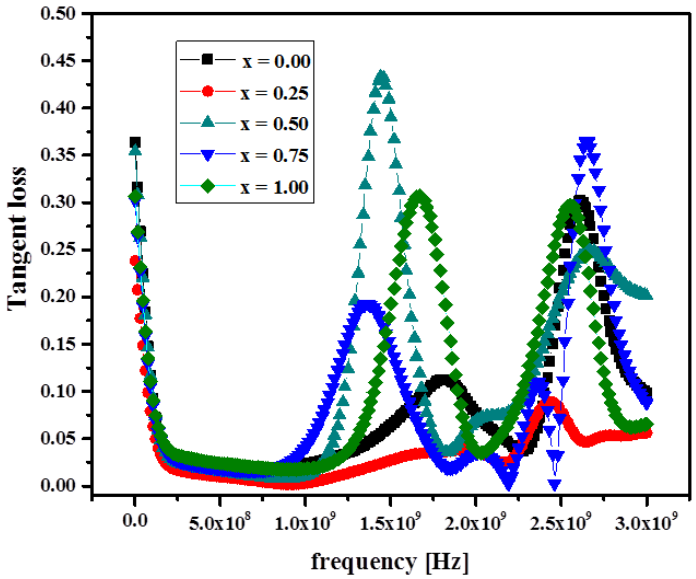

Figure 11. Effect of Frequency on the Tangent Loss of all Compositions

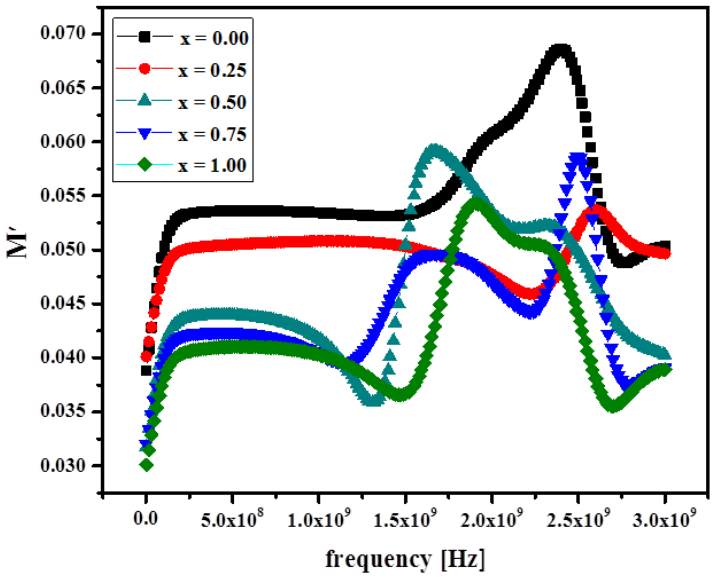

Figure 12. Frequency dependent Real part of electric modulus

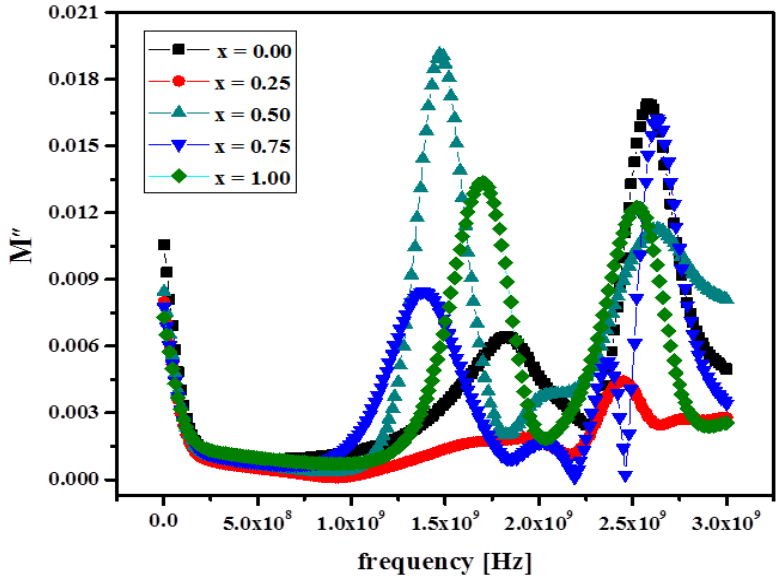

Figure 13. Frequency dependent imaginary part of electric modulus

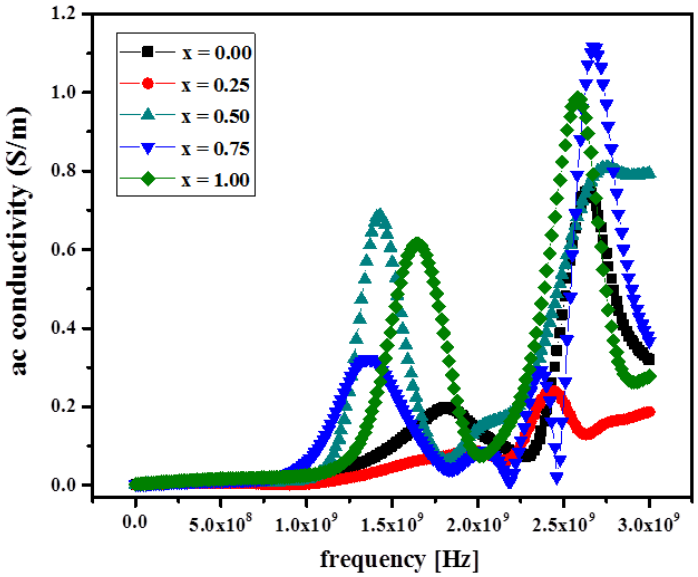

Figure 14. Effect of Frequency on the AC conductivity of all Compositions

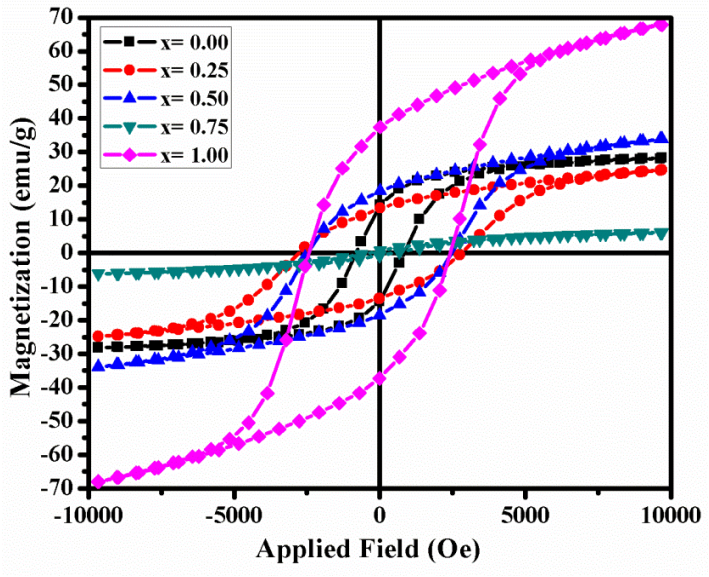

Figure 15. Interpretation of VSM graph of $BaPr_xFe_{12-X}O_{19}$.

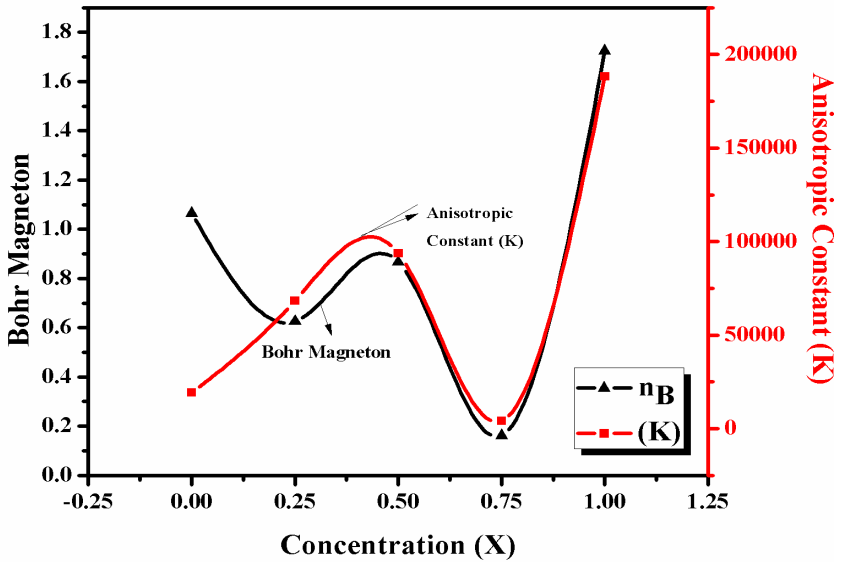

Figure 1. Concentration Verses Bohr magneto and Anisotropic Constant

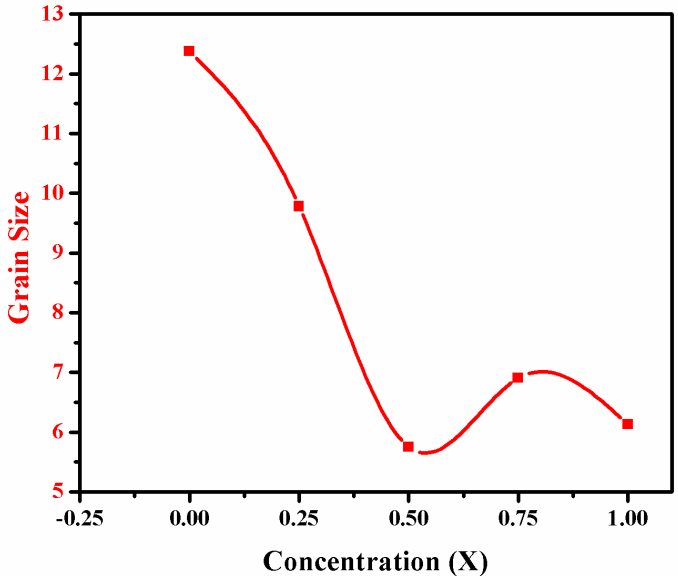

Figure 2 Concentration Vs Grain size

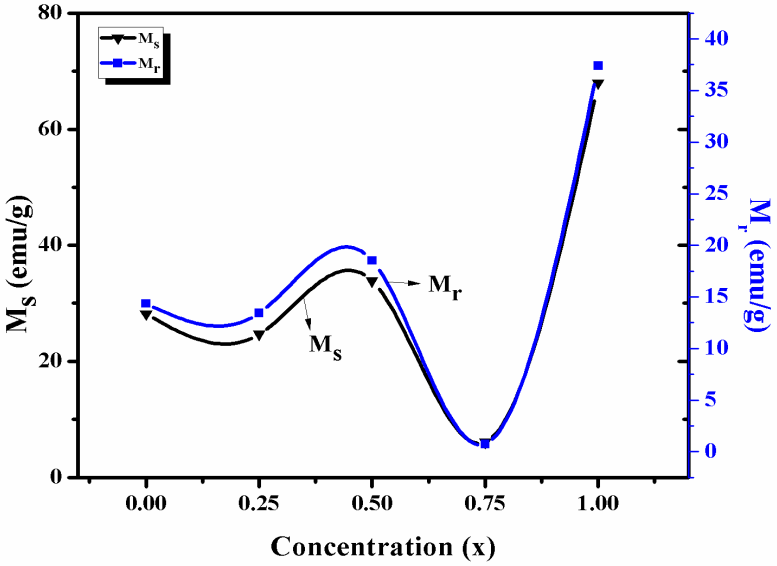

Figure 3. Concentration verses Magnetization Ms and Corecivity H_c

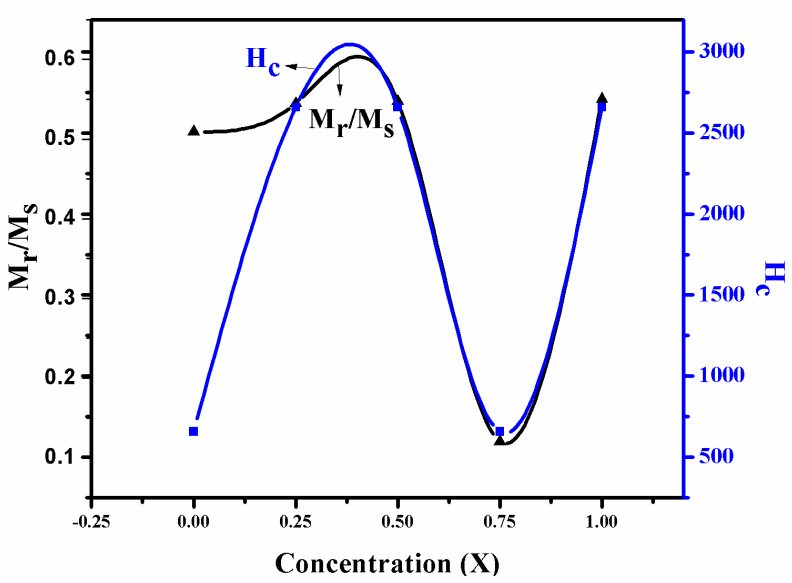

Figure 4 Concentration verses Remanance & Corecivity

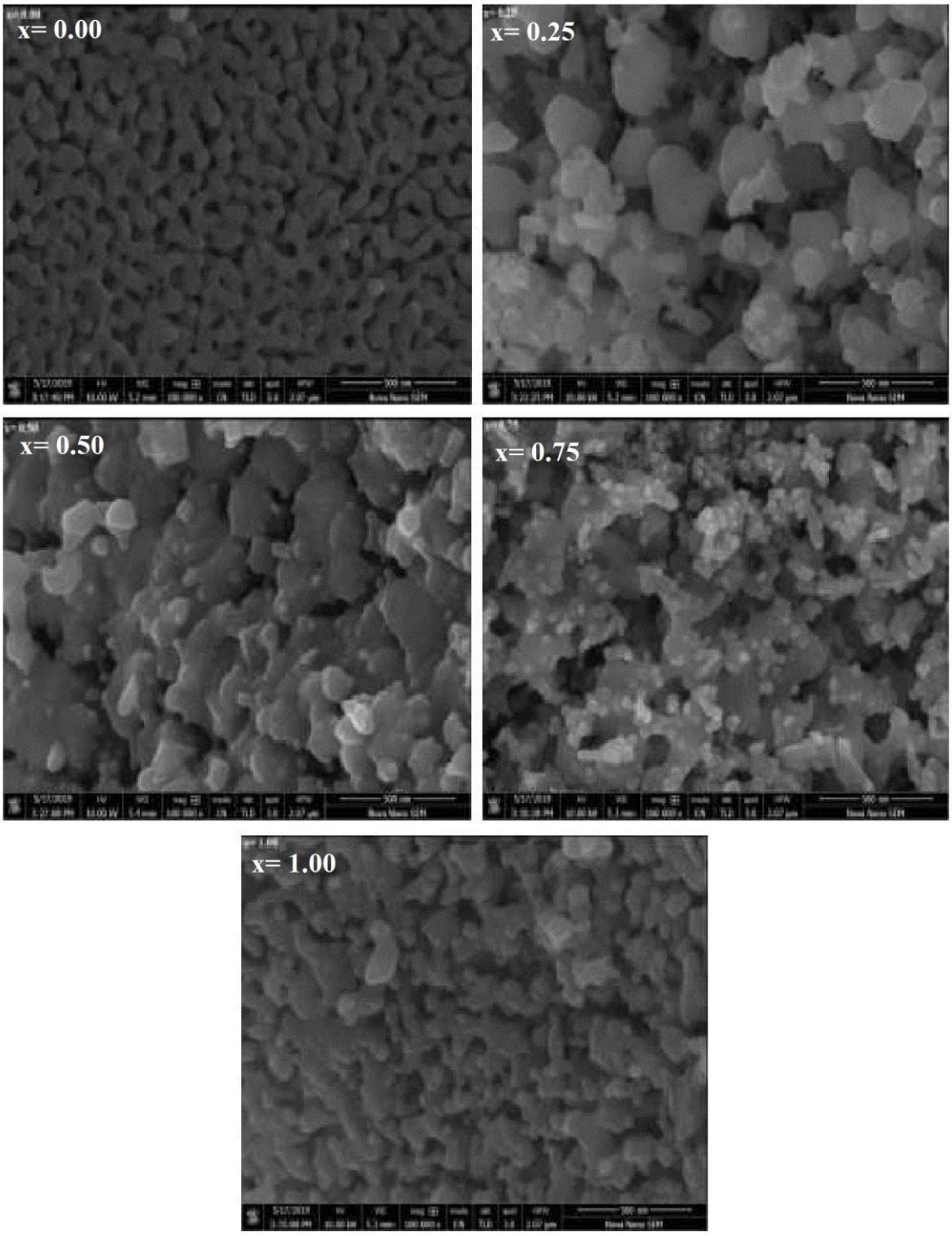

Figure 20: SEM Images of $BaPr_xFe_{12-x}O_{19}$

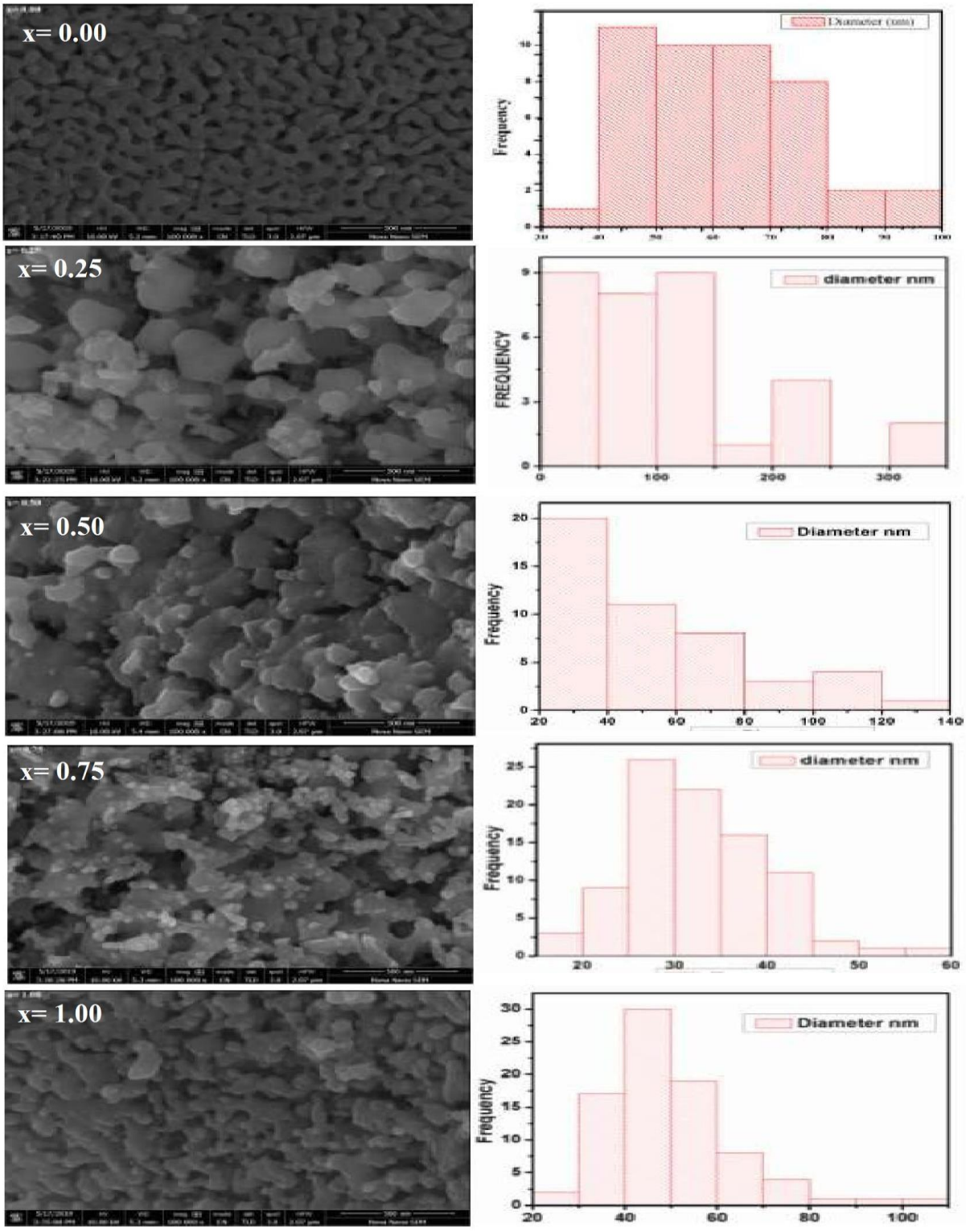

Figure 21: Measurement of Grain size, its diameter, and fitting via Gaussian fitting

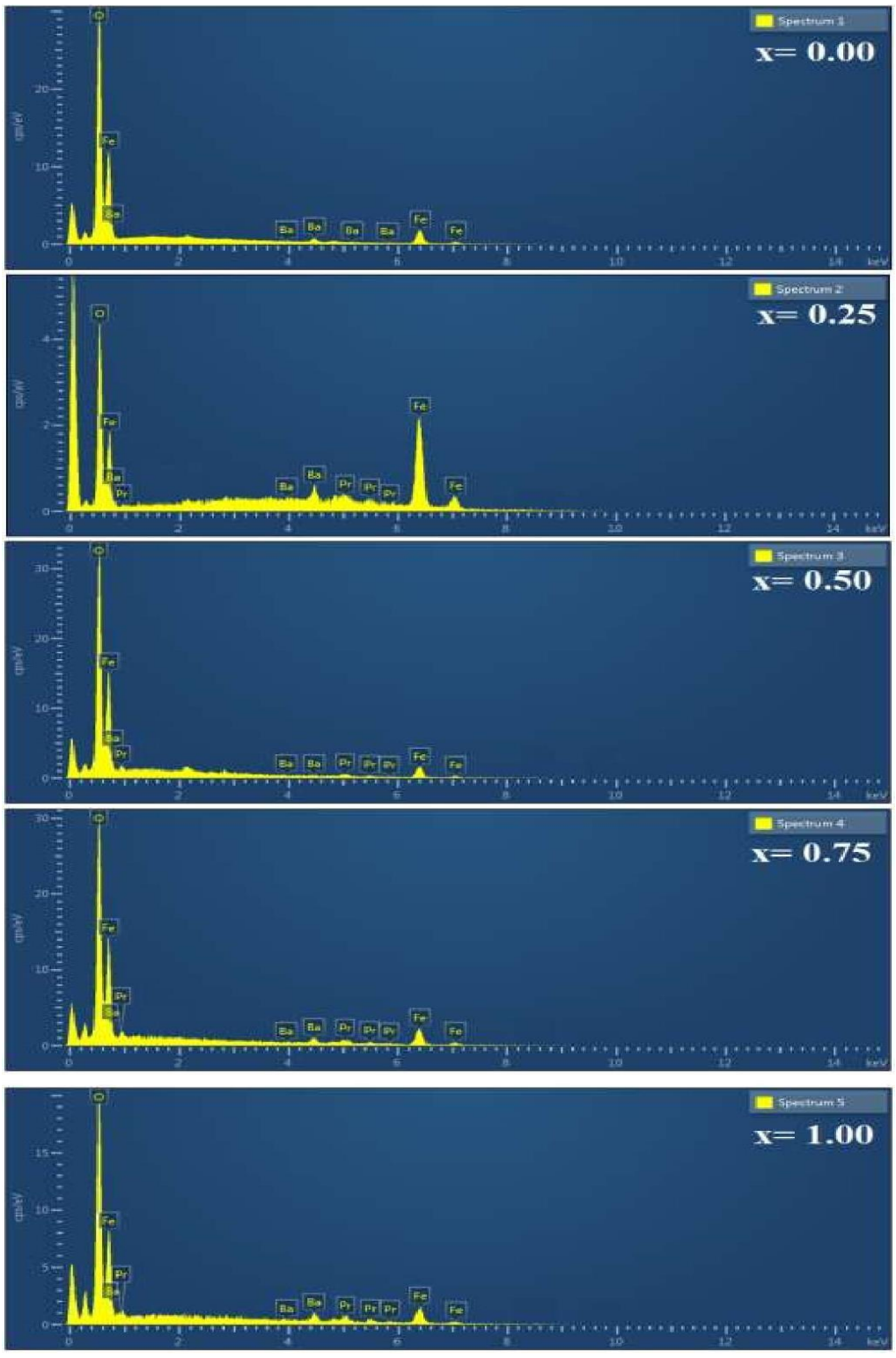

Figure 22: Spectrum Viewer of SEM for $BaPr_xFe_{12-X}O_{19}$

Table 1. Lattice constants, crystal size, volume of unit cell, X-ray density, bulk density, molar weight, stacking fault, lattice and micro strains of $BaPr_xFe_{12-X}O_{19}$(x = 0.0, 0.25, 0.50, 0.75, 1.00).

Concentration (x)	0.0	0.250	0.500	0.750	1.000
Lattice Constant (a)(Å)	5.939	5.874	5.936	6.017	5.836
Lattice Constant (c) (Å)	22.955	23.603	23.368	23.801	23.914
crystal size (nm)	12.376	9.778	5.748	6.903	6.131
volume of unit cell ($a^2c * 0.866$)	701.254	705.301	712.988	746.240	705.375
X-Ray Density (gcm^{-3})	5.264	8.001	8.063	7.846	8.439
Bulk Density (gcm^{-3})	0.181	0.226	0.228	0.227	0.227
Molar Weight	1111.467	1132.733	1153.998	1175.264	1196.530
Lattice Strain	0.0089	0.0087	0.0080	0.0076	0.0059
Micro Strain	0.0030	0.0026	0.0024	0.0023	0.0018
Stacking Fault	0.452	0.450	0.447	0.446	0.448

Table 2. Frequency bands of FTIR analysis of $BaPr_xFe_{12-X}O_{19}$ (x = 0.0, 0.25, 0.50, 0.75, 1.00)

S. No.	Composition	$\nu_1(cm^{-1})$	$\nu_2(cm^{-1})$
1	$BaFe_{12}O_{19}$	424. 75724	518.760647
2	$BaPr_{0.25}Fe_{11.75}O_{19}$	424.097104	518.100511
3	$BaPr_{0.50}Fe_{11.50}O_{19}$	423.436968	517.836457
4	$BaPr_{0.75}Fe_{11.25}O_{19}$	423.172923	517.17632
5	$BaPr_{1.00}Fe_{11}O_{19}$	422.776831	516.912266

Table 3. Dielectric constant, dielectric loss and tangent loss of $BaPr_xFe_{12-X}O_{19}$ (x = 0.0, 0.25, 0.50, 0.75, 1.00)

Parameters	Frequency	x = 0.00	x = 0.25	x = 0.50	x = 0.75	x = 1.00
Dielectric Constant	1MHz	26.09563	26.41887	32.30636	32.44263	35.34441
	1GHz	18.7032	19.6724	23.89976	24.76169	24.80203
	3GHz	19.66109	20.15654	24.14431	25.32894	25.576
Dielectric Loss	1MHz	16.46267	10.82714	19.72476	16.6804	18.29673
	1GHz	0.438129	0.054261	0.221135	0.923055	0.433672
	3GHz	1.774825	1.106516	4.726235	1.87593	1.699014
Tangent Loss	1MHz	0.630859	0.409826	0.610553	0.514151	0.51767
	1GHz	0.023425	0.002758	0.009253	0.037278	0.017485
	3GHz	0.090271	0.054896	0.195749	0.074063	0.06643

Table 4. Real and imaginary parts of impedance, real and imaginary parts of modulus, AC conductivity of $BaPr_xFe_{12-X}O_{19}$ (x = 0.0, 0.25, 0.50, 0.75, 1.00)

Real part of impedance (Z')	1MHz	21102.8	16208.2	16800.1	15296.2	14096
	1GHz	1.51899	0.17014	0.46974	1.82426	0.85522
	3GHz	1.85256	1.10452	3.17622	1.18294	1.0519
Imaginary part of impedance (Z")	1MHz	33450.8	39549	27516.3	29750.4	27229.7
	1GHz	64.8439	61.6826	50.7683	48.9373	48.9107
	3GHz	20.5222	20.1202	16.226	15.9721	15.8347
Real part of modulus (M')	1MHz	0.027411	0.032408	0.022548	0.024379	0.022313
	1GHz	0.053437	0.050832	0.041838	0.040329	0.040307
	3GHz	0.050451	0.049463	0.039889	0.039265	0.038927
Imaginary part of modulus (M")	1MHz	0.017293	0.013282	0.013767	0.012534	0.011551
	1GHz	0.001252	0.00014	0.000387	0.001503	0.000705
	3GHz	0.004554	0.002715	0.007808	0.002908	0.002586
AC Conductivity	1MHz	3.96964E-6	2.61074E-6	4.75622E-6	4.02214E-6	4.41188E-6
	1GHz	1.06244E-4	1.31581E-5	5.36243E-5	2.23837E-4	1.05163E-4
	3GHz	0.00128	8.00441E-4	0.00342	0.00136	0.00123

Table 5. Saturation magnetization, retentivity, coercivity, squareness ratio, Bohr magneton and anisotropic constant for BaPrxFe12-X O19 (x = 0.0, 0.25, 0.50, 0.75, 1.00)

Concentration (x)	0	0.25	0.5	0.75	1
Magnetization (Ms) (emu/g)	28.175	24.678	33.841	6.060	67.956
Retentivity (Mr) (emu/g)	14.351	13.444	18.529	0.729	37.407
Corecivity (Hc) (Oe)	656.278	2658.420	2658.420	656.278	2658.420
Squareness Ratio (M_r/M_s)	0.509	0.545	0.548	0.120	0.550
Bohr Magneton (n_B)	1.065	0.626	0.867	0.163	1.725
Anisotropic Constant (K) (J/m^3)	19261.290	68338.094	93712.590	4142.996	188183.739

Table 6: values of doped material be Spectrum for $BaPr_xFe_{12-X}O_{19}$ (x = 0.0, 0.25, 0.50, 0.75, 1.00)

Concentration (x)	0	0.25	0.5	0.75	1
O	12.54	5.1	11.86	11.07	9.99
Fe	5.76	19.97	4.64	6.23	4.99
Ba	0.75	1.65	0.71	1	1.36
Pr	0	1.2	0.69	1.13	1.95